Chapter 9

HEIGHTS-EUV Package for DPP Source Modeling

A. Hassanein, V. Morozov, V. Sizyuk, V. Tolkach, and B. Rice

Contents

9.1 Introduction

This chapter presents an integrated model that is being developed to describe the hydrodynamic and optical processes that occur in DPP devices for EUVL applications. The developed model will eventually address the following subjects: plasma evolution and magnetohydrodynamic (MHD) processes, atomic data and plasma properties, detailed photon radiation transport, and interaction between plasma/radiation and material. Regions with differing propagation speeds of perturbation require accurate numerical solutions of the MHD equations. The total variation diminishing (TVD) scheme in the Lax-Friedrich formulation for the description of magnetic compression and diffusion in a cylindrical multidimensional geometry is the most suitable and is used in our model. Depending on the complexity of the problem and the availability of computer time, a combination of various atomic and plasma models is being developed for populations of atomic levels, ion concentrations, plasma properties, and opacities. These include a collisional radiation equilibrium plasma model, a Hartree-Fock (HF) self-consistent-field atomic model, and a Hartree-Fock-Slater (HFS) method with splitting of atomic levels. Because of its influence on the whole dynamics of the discharge, radiation transport

for both continuum and lines with detailed spectral profiles is modeled by various discrete-ordinate and Monte Carlo methods. The developed models have been integrated into the HEIGHTS-EUV computer simulation package. The features of the package allow one to study the hydrodynamics and radiation of two-gas mixtures in dense plasma focus (DPF) devices in the presence of impurities and erosion products that can affect radiation output.

The goal of this chapter is to provide an overview of methods and techniques we use to simulate MHD and optical processes that occur in DPP devices of various electrode constructions. The general types of DPP devices that can be simulated within the HEIGHTS-EUV package are schematically shown in Fig. 9.1: (a) the DPF device, (b) the Z-pinch device, and (c) the hollow-cathode triggered pinch plasma source.[1–3] The electrodes are drawn solid and shown in gray. The device is filled with xenon gas under an initial pressure in the range of several tens of millitorr at room temperature, corresponding to an initial density of the gas in the range of 10^{14}–10^{15} cm^{-3}. It is also assumed that a preionization step heats the gas to a temperature of near 1 eV and initiates the discharge.

Typical representatives of the DPP devices are the conduction-type devices. The plasma is an element of the electric circuit, which gets its discharge current from the feeding capacitor C_0. The simulation of the discharge by using the external (experimentally recorded) current may lead to the violation of the self-consistency principle, because the energy balance is not conserved and the plasma dynamics can be distorted. The physical processes that take place in these DPP devices are identical and can be described within the same mathematical model. The distinguishing features of each particular design can also be affected by the initial and boundary conditions, such as the design and geometry of solid walls, the initial plasma parameters, the parameters of the electric circuit, and the methods of

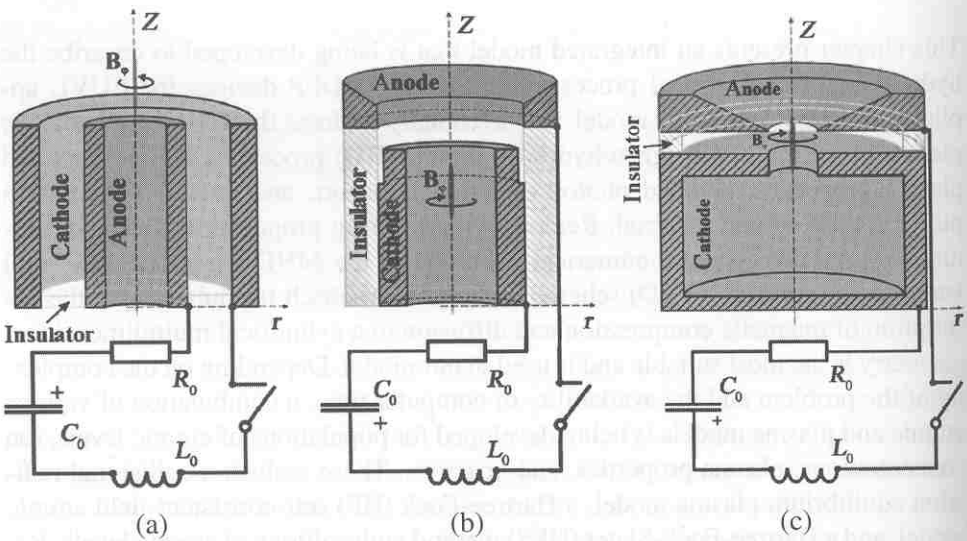

Figure 9.1 Schematics of DPP devices.

turning the device on and off. The MHD processes, radiation transport, and thermal conduction are implemented as a part of the HEIGHTS-EUV package, while design-specific features are implemented as additional blocks.

9.2 Magnetohydrodynamics

The behavior of a conductive flow in the magnetic field due to the current displacement triggered by the discharge is described by the general set of 3D resistive conservative MHD equations. In modeling such functioning DPP devices as Z-pinch, plasma focus, and Θ-pinch devices, the organization of the correct energy exchange is a key to successful simulation. The energy exchange is determined by the set of different energy transport processes, including magnetic diffusion, thermal conduction, and radiation energy loss.

The plasma is represented by the conservative variables of mass density ρ, momentum density $\rho\mathbf{v}$, total energy density e, and magnetic field $\mathbf{B}$:

$$\frac{\partial \rho}{\partial t} + \nabla \cdot (\rho \mathbf{v}) = 0, \tag{9.1}$$

$$\frac{\partial \rho \mathbf{v}}{\partial t} + \nabla \cdot \left(\rho \mathbf{v}\mathbf{v} + p_{\text{tot}} - \frac{1}{4\pi}\mathbf{B}\mathbf{B} \right) = 0, \tag{9.2}$$

$$\frac{\partial e_{\text{tot}}}{\partial t} + \nabla \cdot \left[\mathbf{v}(e_{\text{tot}} + p_{\text{tot}}) - \frac{1}{4\pi}(\mathbf{v} \cdot \mathbf{B})\mathbf{B} + \frac{c^2 \eta}{16\pi^2}(\nabla \times \mathbf{B}) \times \mathbf{B} \right] = Q_{\text{th}} + Q_{\text{rad}}, \tag{9.3}$$

$$\frac{\partial \mathbf{B}}{\partial t} + \nabla \cdot (\mathbf{v}\mathbf{B} - \mathbf{B}\mathbf{v}) + \frac{c^2}{4\pi}\nabla \times (\eta \nabla \times \mathbf{B}) = 0. \tag{9.4}$$

Equations (9.1)–(9.4) represent the conservation of mass, momentum, energy, and magnetic flux, respectively. If not mentioned otherwise, all values are given in Gaussian units. In the rest of the chapter, the magnetic permeability μ is assumed to be 1. The total energy density is determined as a sum of internal, kinetic, and magnetic energy densities, whereas the pressure term is separated into hydrodynamic and magnetic parts:

$$\begin{aligned} e_{\text{tot}} &= e_{\text{h}} + \frac{\mathbf{B}^2}{8\pi} = e_{\text{int}} + \frac{\rho \mathbf{v}^2}{2} + \frac{\mathbf{B}^2}{8\pi}, \\ p_{\text{tot}} &= p_{\text{h}} + \frac{\mathbf{B}^2}{8\pi}. \end{aligned} \tag{9.5}$$

To complete this full system of MHD equations, functional forms for the thermodynamic pressure $p_{\text{h}} = p_{\text{h}}(e_{\text{int}}, \rho)$ and resistivity $\eta = \eta(e_{\text{int}}, \rho)$ are calculated from the equation of state, discussed below. Details of implementing and solving the set of the MHD equations by the TVD method in the Lax-Friedrich formulation for cylindrical geometries can be found elsewhere.[4–6] The thermal conduction

must be calculated for the gas-plasma environment, the properties of which can significantly vary from point to point. Direct integration of the heat-flux divergence $\nabla\lambda \cdot \nabla T$ within the hydrodynamic scheme can often lead to nonconvergence and disruption of the solution. An alternative approach is to present the divergence term as a heat source Q_{th} and organize, in cylindrical coordinates, a separate thermal conduction scheme:

$$\frac{\partial e_{\text{tot}}}{\partial t} - \frac{1}{r}\frac{\partial}{\partial r} r\lambda \frac{\partial T}{\partial r} - \frac{\partial}{\partial z}\lambda \frac{\partial T}{\partial z} = 0, \tag{9.6}$$

$$Q_{\text{th}} = \frac{\partial e_{\text{tot}}}{\partial t} = \nabla\lambda \cdot \nabla T, \tag{9.7}$$

where Q_{th} is the energy correction to the energy Eq. (9.3), and $\lambda = \lambda(e_{\text{int}}, \rho)$ is the thermal conductivity.

In the evolution of the plasma pinch, the temperatures of the plasma can vary within the broad range from fractions of an electron volt to hundreds of electron volts. At such different temperatures, several mechanisms can contribute to the thermal conductivity. At low temperatures with low charge state, the classical elastic scattering by neutral atoms gives the main contribution to the total thermal conductivity. Correction is needed to allow for the dependence of the atom diameter on the energy of impact. At higher ionization states, an ambipolar diffusion—the diffusion of the neutral atoms in the plasma—contributes to the total value. When a neutral atom appears in the hot area, it is ionized, losing energy equal to the ionization energy. At still higher ionization states, the electronic thermal conduction is a main contributor, which is given by the classic Spitzer formula with the correction for nonideality of the plasma. Similarly, we can also calculate the ionic thermal conduction, but it is substantially weaker than the electronic conduction. The process of energy transfer by the photons emitted from the hotter areas and absorbed by the colder ones is included directly in the form of radiation transport, as described below.

In view of the cylindrical symmetry of a DPP device, we wrote the general set of MHD Eqs. (9.1)–(9.4) in cylindrical coordinates (r, φ, z); we neglected the plasma motion in the φ direction and assumed that the magnetic field had only one component B_φ. These simplifications allowed us to reformulate the problem in coordinate form, which provided efficient numerical implementation and various easily implemented enhancements.

The design features and the conditions of a particular EUV source are described in the form of boundary conditions.[5,7] In simplified form, one may subdivide these conditions into three major parts:

- *Hydrodynamic* conditions are set on the boundaries of the hydrodynamic domain and include the condition of free pass, the conditions on the inflow and outflow, and the condition of the symmetry of the device.

- *Magnetic* conditions are set on the magnetic field and include the condition of the driven current in the electric circuit in the area of the feeding voltage, the condition at the conductive walls, and the condition at the axis of symmetry to provide the cylindrical symmetry of the magnetic field.
- *Thermal conduction* conditions are set at the boundaries of the domain and include the given temperature of the wall, the condition of the insulating wall, and the conditions of incoming and outgoing heat flux.

9.3 External Electric Circuit

The most important factors in initiating and governing the plasma discharge in a DPP device are the design and parameters of the external electric circuit. As shown in Fig. 9.2, the electric circuit is normally represented by a set of three elements: the direct conductance C_0, the resistance R_0 of the wires, and the parasitic inductance L_0. The circuit is incorporated into the MHD, where the DPP device is given by its resistance R_{DPP} and inductance L_{DPP}. Since the plasma parameters depend upon the whole dynamics of the discharge, they provide feedback from the MHD to the electric circuit, changing the behavior of the current as a function of time.

The voltage drop in the DPP device is caused by the induced and the ohmic voltages. The inductance of the DPP device can be expressed by the Faraday law, which describes an induced voltage caused by the change of the magnetic flux. The resistance losses of the device are calculated from the Joule heating. Finally, the distribution of the continuous current in the electric circuit is regulated by the Kirchhoff law, which can be written for the voltage on a capacitor as a function of time. Being incorporated into the general set, the electric-circuit equation is solved self-consistently with the MHD in the form

$$U(t) = \frac{\partial}{\partial t} L_0 I(t) + R_0 I(t) + \frac{\partial}{\partial t} L_{\mathrm{DPP}} I(t) + R_{\mathrm{DPP}} I(t),$$
$$\frac{\partial U(t)}{\partial t} = -\frac{I(t)}{C_0}. \tag{9.8}$$

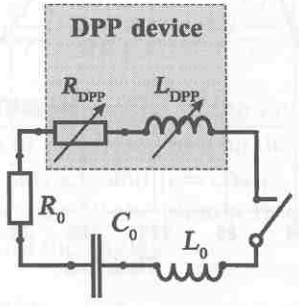

Figure 9.2 Schematic of electric circuit for a typical DPP device.

Figure 9.3 shows results of HEIGHTS simulation of the current for various DPP devices. In general, the dynamics of the process is described similarly for most devices, despite the differences in design and initial conditions of simulated devices and experimental facilities.

9.4 Detailed Radiation Transport

If the density of the excited particles in the plasma is high enough, one of the substantial mechanisms of heat exchange is radiation transport. The transfer of radiant energy takes place only when the mean free path of a photon corresponding

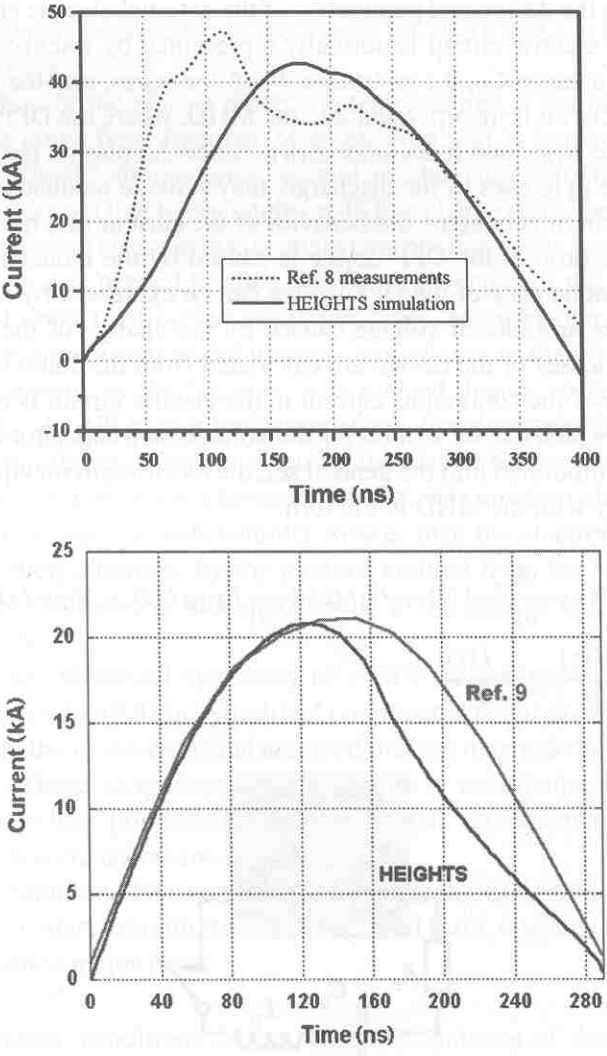

Figure 9.3 Experimental (from Ref. 8) and calculated (from Ref. 9, HEIGHTS) current profiles.

to the center of the emitting line is much less than the size of the hydrodynamic domain. In such a condition the radiation transfer is carried out by those photons, the frequency of which corresponds to the wings of the emitting lines and results in the absorption in colder areas of those photons emitted from the hotter plasma parts.

In studying the transfer of the radiant energy, one needs to distinguish two aspects of the modeling of a DPP device. First, solving the hydrodynamic part of the problem requires correction (redistribution) of the plasma internal energy and, accordingly, correction of the evolution of the whole pinch dynamics. The key is the accurate and detailed calculation of the radiant energy redistribution in the whole plasma domain over the very broad spectral range of participating photons. The second aspect is the detailed calculation of the effective radiation of the EUV source within the operating energy range of 13.5 nm ±2%. In this case, the calculation of the radiation transport must be restricted to take account of only those photons whose energies are in the mentioned range.

In numerical simulation of the radiation transport processes, the radiant energy flux is calculated by integrating the radiation transport equation (RTE),[10,11] which represents the conservation of emitted and absorbed energy along the direction of the transfer. Deterministic transport methods divide the computational domain in space, energy, and angles.[12] The radiation intensity along each direction is determined by integrating the RTE, and the directions are given by the angles of the chosen numerical quadrature. In contrast to the direct resolution of the integro-differential RTE, where one calculates a continuous function of the radiation intensity, the probabilistic model of the energy redistribution operates in discrete ranges of the radiative energies.[11] Given the importance of the correctness and the accuracy of the radiation transport, we are using both methods to ensure and benchmark the validity of our simulation.

At each point of the MHD zone, the local temperature T, the Planck function I_P, and the optical coefficients κ_{emi} and κ_{abs} of emission and absorption of the photon with energy E determine the specific intensity of radiation. To solve for the radiation transport in axisymmetric cylindrical coordinates (r, z) by the discrete-ordinate method (DRT), the RTE for intensity I_E can be written along the direction s as

$$\frac{dI_E}{ds} = \sin\theta\left(\mu\frac{\partial I_E}{\partial r} + \frac{1-\mu^2}{r}\frac{\partial I_E}{\partial \mu}\right) + \cos\theta\frac{\partial I_E}{\partial z} = \kappa_{emi} I_P - \kappa_{abs} I_E. \tag{9.9}$$

Here, θ is the angle between the direction of the ray (s) and the z axis, φ is the angle between the projection of the direction s on the plane perpendicular to z and the normal to the cylindrical surface, and $\mu = \cos\varphi$. The intensity in the direction s is calculated by integration over all the photon frequencies. The net flux $\mathbf{S}_{rad}$ is obtained by integrating over all the angles:

$$\mathbf{S}_{rad} = \int\left[\int_0^{2\pi}\delta\varphi\int_0^{\pi} I_E(\theta,\varphi)\cos\theta\sin\theta\delta\theta\right]dE. \tag{9.10}$$

Finally, the radiation energy loss in each cell is found from $Q_{\text{rad}} = \nabla \cdot S_{\text{rad}}$. Essentially, this method is the result of finite-differencing of the directional dependence of the RTE. Integrals over solid angles are approximated by numerical quadrature, the choice of which defines the directions of the DRT. The solution is carried out simultaneously with the energy-balance solution to provide the distribution of the local energy source, temperature, and density profiles. The method is time-consuming and resource-intensive. This makes it difficult to conduct a parametric study of a DPP device in practice.

Alternatively, the Monte Carlo-based radiation transport (MCRT) method handles and analyzes the discrete portions of the radiant energy separately. Studying the trajectory and the behavior, as well as the number, of emitted and absorbed photons in the test energy groups at each point of the plasma domain (or at the points that present the major interest), one may evaluate the redistribution of the energy due to photon transport. The energy and the trajectory of photon movement are determined by the Monte Carlo technique. It is supposed that each portion is a monochromatic set of photons. The total energy of a portion is a sum of the energies of the component photons, and the portion is called a *macrophoton* or *photon bundle*. The number of test photon bundles is determined by the hydrodynamic parameters of a cell and analyzed by the MCRT method. The energies of the bundles are distributed according to the emission coefficient of the cell. Later on, the history, the behavior, and the paths of the photons are statistically accumulated in the form and energy redistribution within the domain.

To calculate the number N of photons emitted within the spectral range $[E_{\min}, E_{\max}]$ by a domain of volume V per unit time, the emission coefficient $\kappa_{\text{emi}}(T, \rho, \varepsilon)$ needs to be integrated with the Planck function over total spectrum of energies ε:[13]

$$N = V \int_{E_{\min}}^{E_{\max}} \frac{\kappa_{\text{emi}}(T, \rho, \varepsilon)\varepsilon^2}{\hbar^3 \pi^2 c^2} \left(e^{\varepsilon/T} - 1 \right)^{-1} d\varepsilon. \tag{9.11}$$

Here, as elsewhere below, we use traditional notation for the Planck constant $\hbar$ and speed of light c. The energy of the photon is calculated accordingly to the probability density, which in turn is expressed through the emission of the cell. After moving through the domain, the photon can be absorbed as described by the absorption probability density, which grows exponentially with the photon mean free path. Finally, the correction Q_{rad} in the energy Eq. (9.3) due to radiation transport is found, knowing the number and the energy of emitted and absorbed photons in each cell of the hydrodynamic domain:

$$Q_{\text{rad}} = \sum_{i}^{N_{\text{abs}}} \varepsilon_i - \sum_{j}^{N_{\text{emi}}} \varepsilon_j. \tag{9.12}$$

To improve the efficiency of the method, we utilize weight factors of the statistically collected events. Based on the emission of the cells, the first factor is used

to rebalance the number of emitted photons from the less-emitting cells in favor of the most-emitting cells. The accuracy of the computation is regulated by the maximal number N_{max} of photons emitted from a cell. Another weight factor is used to avoid tracking those photons that are emitted and immediately absorbed within the same cell.

The comparative results on the accuracy of DRT and MCRT methods are shown in Fig. 9.4 for typical temperature and density distributions, obtained from the simulation of a Cymer-like device. Both the quantitative and the qualitative behavior of the radiation flux are the same, despite the Monte Carlo method being significantly

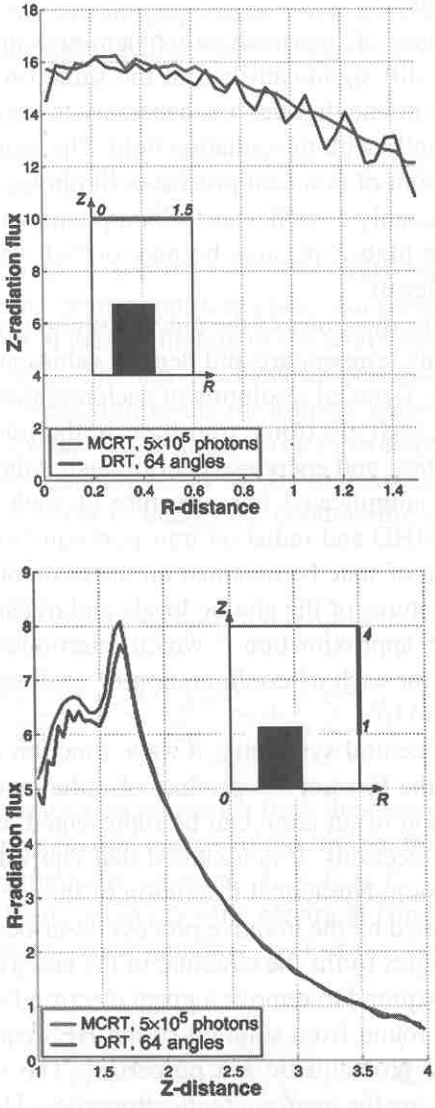

Figure 9.4 Accuracy of HEIGHTS calculations for radiation transport (arb. units).

faster by approximately a factor of 300. This also confirms the high accuracy and reliability of the implementation of the methods.

9.5 Atomic Physics and Opacities

Several studies[14,15] report that radiative emission and transport play a key role in the dynamics and energy balance of laboratory plasmas. In recent years, other studies[16,17] have shown that the high-temperature, moderate-density plasma is not in local thermodynamic equilibrium (LTE), and the radiative properties of plasmas that are optically thick to line radiation are not well described by either coronal or Saha–Bolzmann models.

Normally, in the case of intermediate temperatures and densities, when collisional processes are still significant but, at the same time, radiative effects become apparent and are not negligible, it is necessary to solve the system of kinetic equations self-consistently with the radiation field. The model in its self-consistent formulation takes account of nonlocal processes of photoexcitation and photoionization, and that significantly complicates the computations. The problem becomes particularly difficult for high-Z plasmas because of their very large number of ionization and excitation levels.

The simulation of the dynamics of the pinch evolution is a typical problem with a wide range of working temperature and density values and so with a very complicated ionic structure. Detailed resolution of each possible level for each possible ion, and consequently each electronic transition in the ion, over the wide ranges of temperatures, densities, and energies is enormously laborious, especially when taking account of the complicated fine structure of each split level. Thus, consistent solving of the MHD and radiation transport equations requires the plasma properties and equation of state be obtained on the basis of simplified methods of calculation for the structures of the atomic levels and transition probabilities. One such method is the HFS approximation,[18] which determines the energies and other atomic characteristics for each nl configuration of each ion that might appear in the plasma.

In the condition of central symmetry, a wave function of an N-electron atom can be represented in the form of the product of radial and angular constituents. The radial wave function of an atom can be represented as the product of radial wave functions of the electrons. It is assumed that equivalent electrons have the same radial wave function. Numerical resolution of the HFS equation for each nl configuration is performed by the iterative process described in Ref. 19. The set of calculated binding energies forms the structure of the energy levels, and each value represents the energy required to remove a given electron from the atom.

The wave function found from solution of the HFS equations can be used to calculate energetic and probabilistic ion properties. The wavelengths and spin-orbit splitting constants are the main energetic properties. The probabilistic properties, such as oscillator strengths and photoionization cross sections, are expressed

through the matrix elements of two or more radial wave functions of participating initial and final states.

This study utilizes the description of populations of atomic levels by a collisional-radiation equilibrium (CRE) formulation, which is equally applicable to the limited cases of temperature ranges and intermediate-temperature intervals, because it includes both collisional and radiative effects. The fact that the CRE model considers the transitions between all atomic levels is of particular importance. Nonlocal effects are allowed for by an escape factor,[20] which neglects photoexcitation in the continuum and reduces the strength of spontaneous transitions. Such an approximation is a fair description of the plasma behavior under conditions when an external source of hard radiation is absent.

The plasma ionization state and population levels n for a prescribed set of temperatures and densities are calculated by solving the system of kinetic equations in stationary form:

$$\frac{dn_i}{dt} = -n_i \sum_{j \neq i} K_{ij} + \sum_{i \neq j} n_j K_{ji} = 0. \tag{9.13}$$

Collisional electron excitation and deexcitation, collisional electron ionization, three-body recombination, spontaneous transition, and photo- and di-electronic recombination are included in the calculation of the total rates of electron transition, K_{ij}, from level i to level j. The ion and electron concentrations N_i and N_e are found from the known population levels for a given temperature and substituted into a set of equations of state. Generally, a two-temperature approximation for the pressure p contains corresponding terms for the kinetic energies of ions and electrons. The equation for the internal energy e_{int} contains the terms for ionization and excitation of electrons:

$$\begin{aligned} p &= kT_i \sum_i N_i + kT_e N_e, \\ e_{\text{int}} &= \frac{3kT_e N_e}{2\rho} + \frac{3kT_i \sum_i N_i}{2\rho} + \frac{1}{\rho} \sum_i N_i (R_i + Q_i), \end{aligned} \tag{9.14}$$

where R_i is the sum of ionization potentials from the neutral atom to the $(i-1)$th ion, and Q_i is the mean excitation energy of the ith ion. In our approximation, the electron and ion temperatures are set equal: $T_e = T_i = T$.

The reciprocal of the resistivity η—the electrical conductivity σ—is the sum of conductivities σ_c and σ_n corresponding to electron scattering on charged and neutral particles[21,22]:

$$\eta = \frac{1}{\sigma} = \frac{1}{\sigma_c} + \frac{1}{\sigma_n}, \qquad \sigma_c = \frac{4\sqrt{2}}{\pi\sqrt{\pi}} \frac{(kT_e)^{3/2}\beta}{e^2 Z \Lambda}, \qquad \sigma_n = \frac{3N_e e^2}{\sqrt{2\pi m_e kT_e} N_0 s_0}. \tag{9.15}$$

Here, we use standard notation for the Coulomb logarithm Λ, concentration of neutral atoms N_0, electron charge e, and mean ion charge Z. The parameter β is an electron-electron scattering correction.[22] Empirical values of the transport cross sections s_0 are taken from Ref. 23.

The computational accuracy and completeness of calculated opacities depend upon the accuracy and completeness of the atomic data (such as electronic wave functions, energy levels, transition probabilities, oscillator strengths, and other derived values) and populations of atomic levels. As earlier shown in Refs. 5, 6, 24, and 25, taking account of the electrostatic and spin-orbit splitting of atomic shells and spectral lines may influence the quantitative and qualitative characteristics of radiation transport effects and the dynamics of the energy balance in the plasma. Self-consistent-field methods such as the Dirac-Fock (DF) or HF are believed to be the most accurate and practical atomic methods.[26,19] However, the very large number of energy levels limits their applicability for plasma calculations.

A method for calculating the optical coefficients for high-Z plasmas within the CRE model was developed and implemented in Ref. 24. The distinguishing feature of the method is the joint use of HFS atomic data and Racah techniques for angular moments. The splitting of a configuration is interpreted as a switch to the energy level being dependent on the quantum numbers L, S, and J, as well as on the quantum numbers that uniquely specify the energy of a term. With the first-order approximation of perturbation theory, one can obtain the energetic corrections that give the energy of electron interaction[27]:

$$E = \sum_k F_k(nl, nl) f_k + \sum_k F_k(nl, n'l') a_k + \sum_k G_k(nl, n'l') b_k. \tag{9.16}$$

The three terms on the right side express respectively the interaction between equivalent electrons inside the shell and the direct and exchange electron interactions for the nl and $n'l'$ shells. The expressions for the Slater integrals F_k and G_k and the angular factors f_k, a_k, and b_k are rather complex and can be found in the literature on the theory of atomic structure.[27,28]

Spin-orbit splitting results in either one-particle interaction of the electron's spin with its own orbital angular momentum, or the interaction of the total spin of a shell with the total orbital angular momentum of that shell. More complicated effects are neglected. The splitting of unfilled shells with equivalent electrons is given by cumbersome formulas and depends on the type of coupling. We use the LS-coupling approximation, and the spin-orbit splitting is determined by the Landé interval rule[29,30]:

$$\Delta E_J = 0.5 \cdot A \cdot [J(J+1) - L(L+1) - S(S+1)], \tag{9.17}$$

where A is the fine-structure splitting constant.

Numerical implementation of energy-level splitting is done by several procedures, including calculation of optical coefficients of absorption and emission, the

photoabsorption threshold, and the kinetic matrix for generating populations of levels. The procedure of splitting is realized similarly for all mentioned calculations, and its algorithm depends on the type of splitting level. The relative probabilities for split components are calculated from the corresponding oscillator strength of the transition with the help of the Racah technique, as described in Refs. 31 and 24. The assumption that the Boltzmann equilibrium is reached between split components of the same configuration significantly simplifies the calculation of relative populations in that configuration. Then, the ionization state and relative populations of levels can be derived by means of the traditional CRE model for the *nl* shell.

The electronic transitions and their accompanying absorption and emission of photons are subdivided into three types: bremsstrahlung; photoionization from ground, excited, and inner levels; and discrete transitions. The latter are approximated in the form of dipole transitions and include transitions between ground and excited states, transitions between excited states, and, partly, the transitions from inner shells. Because of their importance, the profiles of spectral lines are processed very carefully by means of the major broadening mechanisms such as radiation, Stark, Doppler, and resonance broadening.[32]

The total absorption coefficient κ_{abs} is calculated as a sum of absorption coefficients for free-free (κ_{ff}), bound-free (κ_{bf}), and bound-bound (κ_{bb}) radiation transitions, weighted with the population levels N_{ij}, where index i refers to the ionization state, and index j to the excitation level. The coefficients are explained as

$$\kappa_{\text{ff}}(T, \rho, \hbar\omega) = \sum_i \sigma_i(T, \hbar\omega) N_i(T, \rho) N_e(T, \rho) \left[1 - \exp\left(-\frac{\hbar\omega}{kT}\right)\right],$$

$$\kappa_{\text{bf}}(T, \rho, \hbar\omega) = \sum_i \sum_j \sigma_{ij}(\hbar\omega) N_{ij}(T, \rho), \tag{9.18}$$

$$\kappa_{\text{bb}}(T, \rho, \hbar\omega) = \sum_i \sum_{j,k} \frac{\pi e^2}{m_e c} f_{jk} \Phi(T, \rho, \omega) N_{ij}(T, \rho).$$

Knowing the cross sections of inverse processes, we can calculate the total emission coefficient κ_{emi} by similar formulas. The values of the oscillator strengths f_{jk}, photoionization cross sections σ_{ij}, line profile Φ, and Gaunt factors G_i are given elsewhere.[24,31,33]

The results from computation of the absorption coefficient of the xenon plasma for our simulation density (1×10^{15} cm^{-3}) and temperature (50 eV) are shown in Fig. 9.5. Additionally, detailed resolution is given for several important energy ranges. The computations are from the CRE model with several modifications: continuum absorption, continuum with HFS-line absorption, and continuum with split-line absorption. The width of the frequency interval was comparable to the Doppler width of the strongest spectral lines, which provides satisfactory resolution of line profiles. Major differences are observed in the energy interval from 10 to

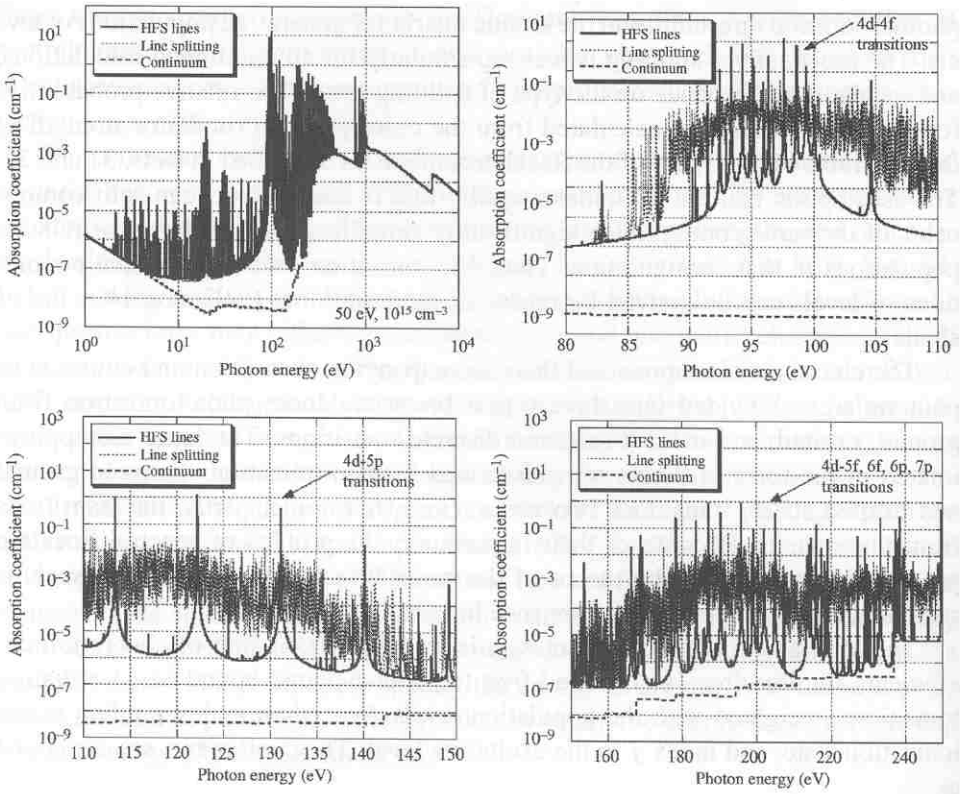

Figure 9.5 Absorption coefficients of Xe plasma at 50 eV and 1×10^{15} cm^{-3}.

3000 eV. At around 100 eV, the lines are split, corresponding to transitions $4d^q$-$4d^{q-1}4f$, $4d^q$-$4d^{q-1}5p$, and $4p^64d^q$-$4p^54d^{q+1}$.

The amplitudes of the split lines are not very high; however, the number of lines is very large, and practically all lines are optically thin in the energy range in question. By our technique, the detailed emission and absorption spectra are initially calculated on a very fine spectral-frequency mesh (up to 100,000 points) for the expected range of MHD values. Because of the large size of the generated opacity tables, the use of such detailed data is impractical, and the emission and absorption coefficients are averaged over spectral groups.

There is no rigorous theory for averaging the opacities over a group of frequencies. Such an averaging procedure may be considered correct only when the absorption coefficient is essentially constant within the group, or the optical thickness of each line is very small, and the absorption becomes a nearly linear function of the frequency. Such a situation is possible only for the continuum, and even in that case, every photoionization threshold must become a boundary of a group. The situation becomes even more complicated for the line spectrum, where the absorption coefficient often exhibits a very deep drop of several orders of magnitude within a very limited frequency interval, say, from the center of a very strong line to the wings of the same line, and the center of the line is optically very thick. More-

over, the temperature and density values may vary; this condition leads to spectral lines from the other ions, and the width of the existing lines also changes.

From a practical viewpoint, an organized selection of several of the strongest lines is a reasonable way to describe optical coefficients in detail within the most important hydrodynamic ranges for typical temperature and density values. The other lines are averaged within broad enough groups. Unfortunately, one does not know the typical values a priori, because the primary goal of the numerical simulation is the determination of the typical hydrodynamic parameters within the important areas of the plasma domain.

For a uniform isothermal plasma, the optical thickness of a spectral line is determined by the multiplication of the absorption coefficient of the line by the linear dimension of the plasma: $\tau(\varepsilon) = \kappa_{abs}(\varepsilon) \cdot l$. In the case of a nonuniform, nonisothermal plasma, this definition is generalized to $\tau(\varepsilon) = \int \kappa_{abs}(T, \rho, \varepsilon) dl$ over the interval Δl, where the ion exits emitting at the frequency ε. The borders of the groups are calculated from the following considerations. First, the width of a group, $\Delta\varepsilon$, should never exceed αT, where T is the plasma temperature and α is some parameter chosen for averaging. This condition provides the smooth averaging of opacities in the continuum region, where the averaging is normally performed within the broad groups, and the optical thickness is significantly less than unity. The second consideration is the requirement of invariability of the optical coefficient at some chosen value β within the group. This condition provides a well-specified resolution of the spectral lines with the optical thickness nearly at unity, and of the wings of the lines with the optical thickness greater than unity. The final consideration is that all those frequencies that belong in the detailed spectrum to a line with $\tau(\varepsilon) \geq 1$ are also included within the borders of the groups. This arrangement provides a very thorough resolution of strong lines in the averaging spectrum. By variation of the parameters α and β, several group mean opacities are generated with different levels of completeness.

Based upon several recent studies,[2,34] it was initially supposed that the maximum radiation transport corresponds to the moment of pinch formation. Typical pinch parameters are the following: the temperature is close to 25 eV, the density is 10^{17} cm^{-3}, the spectral range in radiation energies varies from 5 to 250 eV, and the average optical plasma thickness is 1 cm. We generated two sets of opacities, averaged over 240 and 791 spectral groups. The comparison of the radiation fluxes showed good agreement and allowed us to choose values for the hydrodynamic parameters from the most-emitting areas. After that, we selected 10 typical temperature and density values and generated the optimal scale of spectral groups, after which, combining all scales, the summary energy scale had 3639 energy groups. The result of the self-consistent hydrodynamic and radiation transport calculations with these opacities can also be used for further improvement of the quality of the coefficients. We have calculated and compared the dynamics of the typical DPP device with the opacities averaged over both 791 and 3639 groups. The dynamics of the plasma is left unchanged, signifying that 791 groups is a quite reasonable initial choice. Nevertheless, during the time of formation and evolution of the pinch,

the detailed opacities show a 5% difference between the 791 and the 3639 groups. Such a difference is quite insignificant from the hydrodynamic point of view, but as seen from Fig. 9.6, is important from the point of view of collectible EUV.

In the first mode of modeling, the radiation transport is calculated self-consistently with respect to the magnetic hydrodynamics, as described above. The goal is to obtain the temperature and density distributions for the second mode of modeling: the calculation of the EUV of the source. The second mode utilizes the same radiation transport method, but another set of opacities.

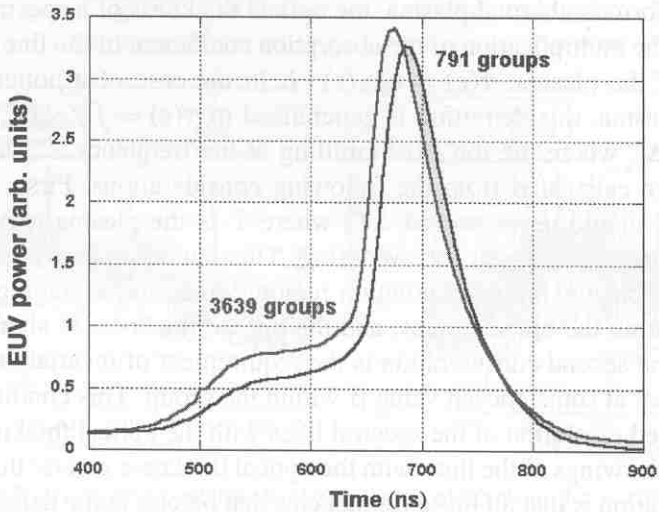

(a)

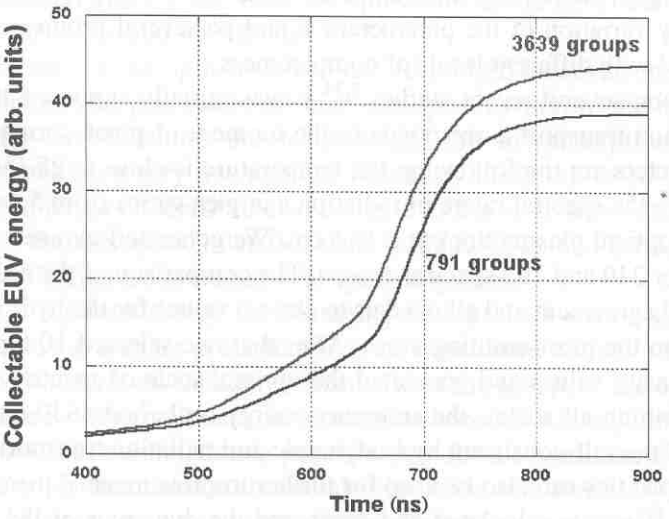

(b)

Figure 9.6 Typical (a) pinch EUV power, and (b) collectible energy, for 791 versus 3639 optical groups.

In using the HFS model for the calculation of energy levels, the typical accuracy of the result is within 10%; this is unacceptable for the EUV range of 13.5 nm ±2%. In contrast with HFS, the more accurate HF model treats the upper and lower states as split into components, and each component is a set of levels with different quantum numbers L, S, and J. The values of the splitting can exceed the required 2% of the transition energy. It thus becomes important to know what fraction of the whole transition is situated within the range of interest.

Several well-known HF methods, each of which calculates the energy levels (and transitions) slightly differently, can be implemented for such a narrow range.[30] In the calculation of the lower state, the average term is often approximated, in that all states with different L, S, and J quantum numbers are supposed to have the same radial wave function and eigenvalue. As shown above, the splitting by L, S, and J is defined by Slater integrals and various angular factors, which represent electrostatic, spin-orbit, and exchange interactions. Relativistic corrections are found within the limits of perturbation theory. To calculate the atomic structures of the EUV-emitting ions, we use the mathematically stricter *LSD* HF method.[30] The total energy of a term is found by solving a separate set of HF equations for each ${}^{S}L$ term. Precisely, the method should be called $LS\nu D$ HF, because the total energy for d shells also depends on the seniority number ν. The splitting of a configuration is found later as the difference of the total energies. In contrast to the average-term HF, all *LSD* HF wave functions, eigenfunctions, and Slater integrals depend on the L and S quantum numbers for inner and outer shells. This condition requires longer, but more accurate, computations, and is very important for calculation of the total energies of the atomic levels.

The angular wave functions are normally calculated separately from the radial wave functions by the summation of the electron momenta. As a rule, the two limiting cases are rarely realized in practice, namely, when electrostatic interaction is considered predominant (*LS* coupling) or the spin-orbit interaction exceeds the electrostatic interaction (*jj* coupling). In intermediate cases, the Hamiltonian matrix cannot be written diagonally in any coupling scheme. Therefore, the complete matrix is written by transforming the Coulomb matrix from *LS* representation to *jj* representation. The eigenvalues of the Hamiltonian matrix are found later by numerical diagonalization, and the eigenvector defines the composition (and purity) of the level corresponding to these eigenvalues and eigenvectors. The level is normally called by the name of the largest contribution of the basis terms from the purity vector. Note that the energy levels found within the intermediate coupling never have 100%-pure *LS* or *jj* coupling, and a difference always exists between the level assigned within the intermediate coupling and the level calculated within the pure coupling scheme and accordingly assigned as required by the scheme.

The calculation was performed for $4d^n$-$4d^{n-1}4f$, $4d^n$-$4d^{n-1}5p$, and $4p^6d^n$-$4p^54d^{n+1}$ transitions of Xe IX–XVIII ions. As found, the components of $4d^n$-$4d^{n-1}4f$ do not fall within the 13.5-nm ±2% energy range. The components of

the $4d^n$-$4d^{n-1}5p$ transition for the Xe XI ion can partly cover the range, and the $4p^6d^n$-$4p^54d^{n+1}$ transition of Xe IX–XVIII has a very broad splitting interval, much broader than the required 2% range.

9.6 Results and Discussion

The results of a DPF discharge depend on the detailed physics of the discharge, the geometrical design features of the device, the electric circuit design, the initial conditions in the chamber, and the current profile. As simulated by the HEIGHTS-EUV package, we present the comparative results of detailed simulation of the discharge near the moment of plasma pinch for the typical designs of EUV sources.

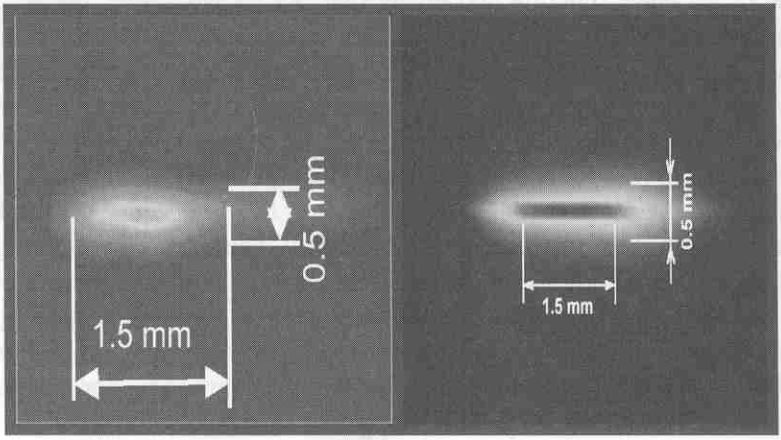

Figure 9.7 Details of the plasma pinch: (left) Ref. 8 experimental study, and (right) the HEIGHTS-EUV simulation.

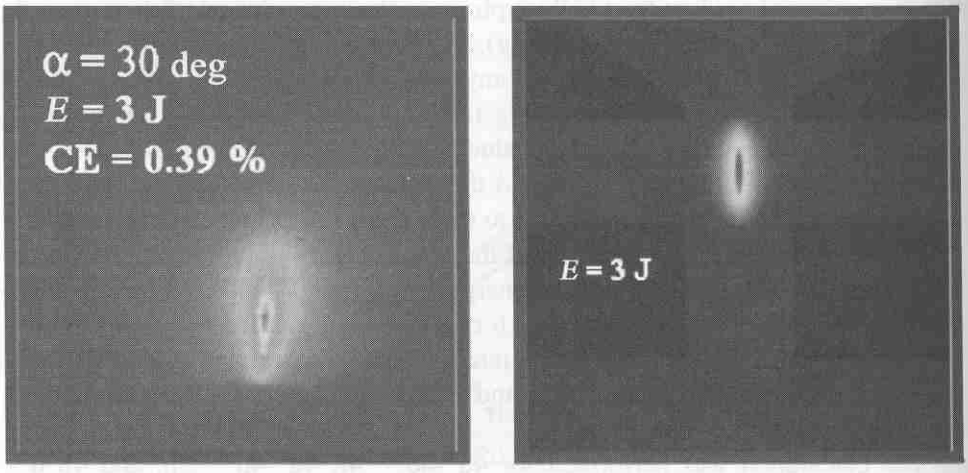

Figure 9.8 Details of the pinch: Ref. 9 experimental study (left) and the HEIGHTS-EUV simulation (right).

The measurements of the pinch, provided in Ref. 8, are in very good agreement with the HEIGHTS simulation, as seen from Fig. 9.7. Similar measurements of the plasma pinch, presented in Ref. 9, agree with our HEIGHTS simulation, as shown in Fig. 9.8.

In optimizing the design of a DPP device, the clear advantage of computer simulation is its flexibility in changing the critical parameters of the discharge. As well known and noted in various studies,[5,8,9] the energy load and the electric circuit parameters are vital to the whole dynamics of the pinch: pinching time, reaching the desired thermodynamic state, and collecting the usable EUV radiation. As shown

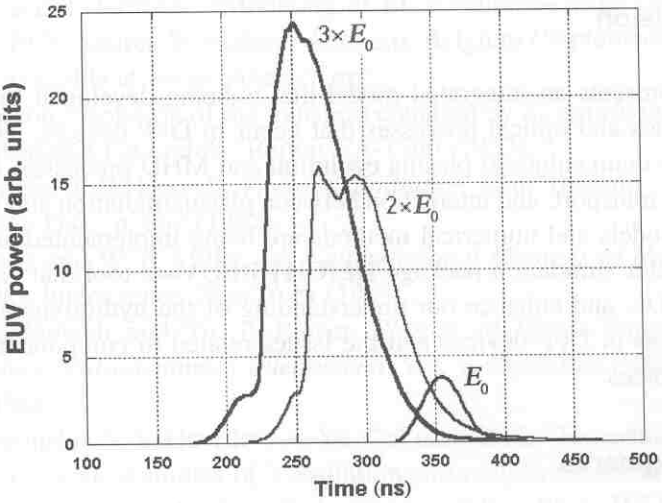

(a)

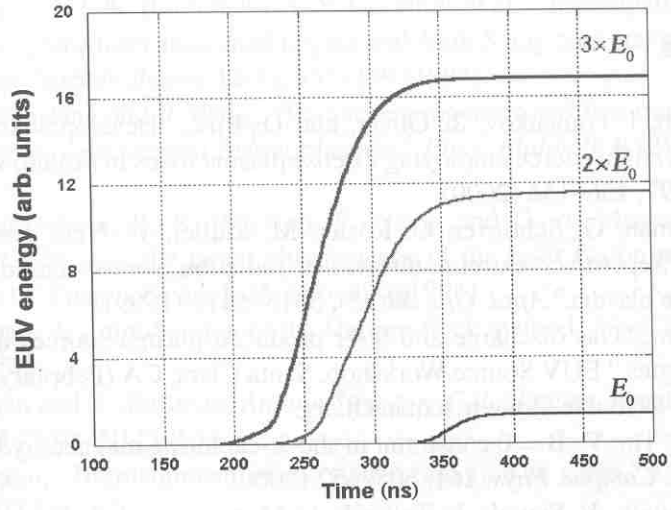

(b)

Figure 9.9 Optimization of the discharge, showing load increase for fixed initial pressure P_0.

in Fig. 9.9, when the energy load is increased, a typical discharge produces higher EUV radiation power and allows collection of more EUV energy. Obviously this is not always true, because when the load is too high, the incoming energy will heat the plasma to higher temperatures so that the concentration of required Xe^{10+} ions becomes low; consequently, less EUV is produced. These calculations give us a hint on how to change the initial plasma parameters: for example, to reduce the pressure to maintain the high EUV collectable energy while reducing the energy input and, as a consequence, reducing the load on the electrodes and stabilizing the EUV source.

9.7 Conclusion

This study presents an integrated model that is being developed to describe the hydrodynamics and optical processes that occur in DPP devices. The model addresses three main subjects: plasma evolution and MHD processes, detailed photon radiation transport, and interaction between plasma/radiation and material. The developed models and numerical methods are being implemented and integrated in the computer simulation package HEIGHTS-EUV—a tool that can be used to study, optimize, and enhance our understanding of the hydrodynamics and radiation processes in DPP devices and the issues related to component erosion and lifetime estimates.

Acknowledgments

The Intel Corporation supported a major portion of this work.

References

1. W. Partlo, I. Fomenkov, R. Oliver, and D. Birx, "Development of an EUV (13.5 nm) light source employing a dense plasma focus in lithium vapor," *Proc. SPIE* **3997**, 136–156 (2000).
2. K. Bergman, G. Schriever, O. Rosier, M. Müller, W. Neff, and R. Lebert, "Highly repetitive, extreme-ultraviolet radiation source based on a gas-discharge plasma," *Appl. Opt.* **38**(25), 5413–5417 (1999).
3. U. Stamm, "Gas discharge and laser produced plasma sources at XTREME technologies," EUV Source Workshop, Santa Clara, CA (February 2003). Proceedings available at www.sematech.org.
4. G. Tóth, "The $\nabla \cdot \mathbf{B} = 0$ constraint in shock-capturing magnetohydrodynamics codes," *J. Comput. Phys.* **161**, 605–652 (2000).
5. A. Hassanein, V. Sizyuk, V. Tolkach, V. Morozov, and B. Rice, "HEIGHTS initial simulation of discharge produced plasma hydrodynamics and radiation transport for EUV lithography," *Proc. SPIE* **5037**, 714–727 (2003).

6. A. Hassanein, V. Sizyuk, V. Tolkach, V. Morozov, and B. Rice, "HEIGHTS initial simulation of discharge produced plasma hydrodynamics and radiation transport for extreme ultraviolet lithography," *J. Microlithography, Microfabrication, and Microsystems* **3**(1), 130–138 (2004).
7. O. Diyankov, I. Glazyrin, and S. Koshelev, "MAG—two-dimensional resistive MHD code using an arbitrary moving coordinate system," *Comput. Phys. Commun.* **106**, 76–94 (1997).
8. XTREME technologies GmbH, "Performance update high power gas discharge EUV source development," EUV Source Workshop, Antwerp, Belgium (September 2003). Proceedings available at www.sematech.org.
9. G. Derra and T. Krücker, "Modeling of EUV sources—what can we expect from it?" EUV Source Workshop, Antwerp, Belgium (September 2003). Proceedings available at www.sematech.org.
10. B. G. Carlson, "Solution of the transport equation by S_n approximations," Los Alamos National Laboratory, Report LA-1599 (1953).
11. R. Siegel and J. R. Howell, *Thermal Radiation Heat Transfer*, Hemisphere, Washington D.C., p. 862 (1981).
12. E. E. Lewis and W. F. Miller, Jr., *Computational Methods of Neutron Transport*, Wiley-Interscience, New York (1984).
13. Ya. B. Zeldovich and Yu. P. Raizer, *Physics of Shock Waves and High-Temperature Hydrodynamics Phenomena*, Vol. 1, Academic Press, New York, p. 464 (1966).
14. I. N. Burdonskii, V. V. Gavrilov, A. Yu. Gol'tsov, et al., "Experimental, numerical, and theoretical studies of X-radiation and radiative thermal conductivity in a dense laser plasma with multicharged ions," *Sov. Phys. JETP* **79**(6), 879–890 (1994).
15. B. N. Bazylev, I. N. Burdonskii, V. V. Gavrilov, et al., "Investigation of energy transfer in plane laser-irradiated targets with high X-ray conversion efficiency," *Laser and Particle Beams* **12**(3), 355–359 (1994).
16. J. J. MacFarlane and P. Wang, "Radiative properties and line trapping effects on post-explosion inertial fusion plasmas," *Phys. Fluids B* **3**(12), 3494–3504 (1991).
17. J. J. MacFarlane, R. R. Peterson, P. Wang, and G. A. Moses, "Radiation transport effects in the target chamber gas of the laser fusion power reactor SIRIUS-P," *Fusion Technol.* **26**, 886–890 (1994).
18. J. C. Slater, A simplification of the Hartree-Fock method, *Phys. Rev.* **81**, 385–390 (1951).
19. F. Herman and S. Skillman, *Atomic Structure Calculations*, Prentice-Hall, Englewood Cliffs, NJ (1963).
20. T. Holstein, "Imprisonment of resonance radiation in gases," *Phys. Rev.* **72**, 1212–1233 (1947).
21. L. Spitzer, *Physics of Fully Ionized Gases*, Wiley-Interscience, New York (1962).

22. N. N. Kalitkin, "Properties of matter and MHD programs," M. V. Keldysh Institute of Applied Mathematics, Moscow, Preprint 85 (1985) (in Russian).
23. L. Huxley and R. Crompton, *The Diffusion and Drift of Electrons in Gases*, Wiley-Interscience, New York (1974).
24. V. Tolkach, A. Hassanein, and V. Morozov, "Development of comprehensive models for opacities and radiation transport for IFE system," Argonne National Laboratory, Report ANL-ET/02-23 (2002).
25. H. Würz, S. Pestchanyi, I. Landman, B. Bazylev, V. Tolkach, and F. Kappler, "A 2-D numerical simulation of ITER-FEAT disruptive experiments," *Fusion Sci. Technol.* **40**(3), 191–246 (2001).
26. H. A. Bethe, *Intermediate Quantum Mechanics*, Walter Benjamin, New York, p. 276 (1964).
27. A. P. Jucis and A. J. Savukynas, *Mathematical Foundations of Atomic Theory*, Mintis Press, Vilnius, p. 480 (1973) (in Russian).
28. C. W. Nielson and G. F. Koster, *Spectroscopic Coefficients for the p^n, d^n, and f^n Configurations*, MIT Press, Cambridge, MA (1963).
29. Von A. Landé, "Termstruktur und Zeemaneffekt der Multipletts," *Z. Phys.* **15**, 189–205 (1923).
30. R. D. Cowan, *The Theory of Atomic Structure and Spectra*, Univ. of California Press, Berkeley (1981).
31. I. I. Sobelman, *Introduction to the Theory of Atomic Spectra*, Pergamon Press, Oxford (1972).
32. H. R. Griem, *Spectral Line Broadening by Plasmas*, Academic Press, New York (1974).
33. I. I. Sobelman, L. A. Vainshtein, and E. A. Yukov, *Excitation of Atoms and Broadening of Spectral Lines*, Springer-Verlag, Berlin (1981).
34. E. R. Kieft, J. J. A. M. van der Mullen, G. M. W. Kroesen, and V. Banine, "Time-resolved pinhole camera imaging and extreme ultraviolet spectroscopy on a hollow cathode discharge in xenon," *Phys. Rev E* **68**, 056403 (2003).

No author biographies were available for this chapter.